

Multi-GPU unsteady 2D flow simulation coupled with a state-to-state chemical kinetics



Michele Tuttafesta^{a,*}, Giuseppe Pascasio^b, Gianpiero Colonna^c

^a Liceo Scientifico Statale “V. Vecchi”, via Grecia 12 - 76125 Trani, Italy

^b DMMM& CEMeC, Politecnico di Bari, via Re David 200 - Bari, Italy

^c CNR-IMIP, via Amendola 122/D - 70126 Bari, Italy

ARTICLE INFO

Article history:

Received 12 October 2015

Received in revised form

29 June 2016

Accepted 6 July 2016

Available online 15 July 2016

Keywords:

GPU and multi-GPU

Euler equations

High enthalpy flows

Flux-vector splitting scheme

State-to-state kinetics

Domain decomposition

ABSTRACT

In this work we are presenting a GPU version of a CFD code for high enthalpy reacting flow, using the state-to-state approach. In supersonic and hypersonic flows, thermal and chemical non-equilibrium is one of the fundamental aspects that must be taken into account for the accurate characterization of the plasma and state-to-state kinetics is the most accurate approach used for this kind of problems. This model consists in writing a continuity equation for the population of each vibrational level of the molecules in the mixture, determining at the same time the species densities and the distribution of the population in internal levels. An explicit scheme is employed here to integrate the governing equations, so as to exploit the GPU structure and obtain an efficient algorithm. The best performances are obtained for reacting flows in state-to-state approach, reaching speedups of the order of 100, thanks to the use of an operator splitting scheme for the kinetics equations.

© 2016 Elsevier B.V. All rights reserved.

1. Introduction

The main difficulty in modeling high enthalpy flows is the presence of strong non-equilibrium, because the flow characteristic time is comparable with that of reactions. The common approach to non-equilibrium is the multi-temperature thermodynamic approximation [1]. This theoretical approach has been developed in the framework of the non-equilibrium irreversible thermodynamics, considering that the relaxation of the distribution in each degree of freedom is very fast while different degrees of freedom are weakly coupled. In this context we have Boltzmann or Maxwell distributions for internal (rotation and vibration) and translational degrees of freedom respectively, each one with its own temperature.

However this approach is not really adequate to describe conditions where the distributions depart from the Boltzmann shape. To investigate this kind of problems, the state-to-state (StS) approach [2], developed for modeling gas discharges [3–5], was adapted to high enthalpy flows in different systems such as the boundary layer during atmospheric entry [6], nozzle expansion [7,8] and shock waves, also including radiation transport [9,10]. The non-equilibrium effects in molecular gases are due to the

strong interaction between vibrational relaxation and chemical reactions, involving preferably highly excited molecules, which population is much higher than a Boltzmann distribution with the same mean energy [11,12].

The main drawback of this method is the large computational resources required, in terms of memory and time, which limit the applications in high enthalpy flow to 1D calculations, while for 2D/3D geometries multi-temperature approach is commonly used, requiring less computational resources, in spite its limits were widely described in the literature [11,13].

Nowadays, growing in computer power has favored the application of the state-to-state model in 2D calculations [14] and recently also in a 3D nozzle [15]. This approach has also been used in DSMC (Direct Simulation Monte Carlo) [16,17] or in the more complex DSMC-QCT (Quasi-Classical Trajectory) [18,19].

As already discussed, the StS approach considerably increases the number of independent species. As an example, in the mixture considered in this work (N_2/N), the multi-temperature model includes only two continuity equations for the species and one for the vibrational temperature, while the StS model needs 69 continuity equations for the species, even if no equation for vibrational energy is necessary, because this quantity is calculated directly from the corresponding distribution. For more complex mixtures this number grows rapidly [15] and, in the presence of ionized gases, the Boltzmann equation for the free electron

* Corresponding author.

E-mail address: micheletuttafesta@libero.it (M. Tuttafesta).

distribution must be considered, together with electronically excited states of atoms and molecules [20].

Insertion of StS models in fluid dynamic codes therefore requires new paradigms for reacting mixtures. A possible strategy is to reduce the dimension of StS model to find simplified models for the vibrational kinetics [12,21,22]. In this paper we are exploring a different approach, trying to develop the calculation of complex kinetics using Graphics Processing Units (GPU), that give promising results for non reactive fluid dynamics [23–26]. However, the use of GPU for reacting flows was limited to small number of species, because the efficiency of GPU's rapidly decreases as the number of species increases. The main limit is the memory required to store kinetic matrices and the poor efficiency of GPU in the solution of linear systems with full matrices [24–26].

In the present paper we have implemented the state-to-state kinetics of N_2/N mixture in the fluid dynamic code described in our previous paper [23], separating the convective flux step from the kinetics one by means of an operator splitting method [24–26]. It is noteworthy that this approach allowed us to get affordable simulations with such a detailed kinetics using 69 species and about 10000 reactions, a task otherwise hardly affordable on a single CPU.

To obtain the best performance from the use of GPU architecture, non-standard approach to the solution of stiff equations has been considered, obtaining speed-up of the order of 100. This opens the possibility of implementing state-to-state calculations in 2D/3D calculations.

2. Reactive fluid dynamic model

In this paper we consider the 2D unsteady Euler equations in the general formulation [27–29]

$$\frac{\partial \mathbf{U}}{\partial t} + \frac{\partial \mathbf{F}(\mathbf{U})}{\partial x} + \frac{\partial \mathbf{G}(\mathbf{U})}{\partial y} = \mathbf{W}(\mathbf{U}) \quad (1)$$

where \mathbf{U} is the vector of conserved variables, $\mathbf{F}(\mathbf{U})$ and $\mathbf{G}(\mathbf{U})$ are the flux vectors in x and y directions respectively and $\mathbf{W}(\mathbf{U})$ is the source term of production rates. For a mixture of S chemical components, the s th one having V_s internal levels, the state-to-state approach considers $N = \sum_{s=1}^S V_s$ independent species. The detailed expansion of the equation (1), for a mixture of N species, is [30,31]

$$\begin{aligned} & \frac{\partial}{\partial t} \begin{bmatrix} \rho_{1,1} \\ \vdots \\ \rho_{1,V_1} \\ \vdots \\ \rho_{S,1} \\ \vdots \\ \rho_{S,V_S} \\ \rho u \\ \rho v \\ \rho e \end{bmatrix} + \frac{\partial}{\partial x} \begin{bmatrix} \rho_{1,1}u \\ \vdots \\ \rho_{1,V_1}u \\ \vdots \\ \rho_{S,1}u \\ \vdots \\ \rho_{S,V_S}u \\ \rho u^2 + p \\ \rho uv \\ (\rho e + p)u \end{bmatrix} + \frac{\partial}{\partial y} \begin{bmatrix} \rho_{1,1}v \\ \vdots \\ \rho_{1,V_1}v \\ \vdots \\ \rho_{S,1}v \\ \vdots \\ \rho_{S,V_S}v \\ \rho uv \\ \rho v^2 + p \\ (\rho e + p)v \end{bmatrix} \\ &= \begin{bmatrix} \dot{\omega}_{1,1} \\ \vdots \\ \dot{\omega}_{1,V_1} \\ \vdots \\ \dot{\omega}_{S,1} \\ \vdots \\ \dot{\omega}_{S,V_S} \\ 0 \\ 0 \\ 0 \end{bmatrix} \end{aligned} \quad (2)$$

where $\rho_{s,v}$ is the gas density of the species s in the v state, p is the gas pressure, u and v are respectively the x and y components of the flow velocity and e is the total energy per unit mass. The system (2) will be closed by a relation between p and e under the approximation of perfect gas. $\rho_s = \sum_v \rho_{s,v}$ is the total density of the component s and the total density is given by $\rho = \sum_s \rho_s$. $\{\dot{\omega}_{s,v}\}$ are the corresponding chemical source terms.

2.1. Thermodynamic model

To close the system we need a relation between the energy density, e , and the gas temperature, T , entering the ideal gas equation and the expression of rate coefficients. Denoting with h and ε the enthalpy and the internal energy per unit mass, we have $\rho h = \rho \varepsilon + p$, leading to the following equation

$$\rho (h_{tr} + \varepsilon_{vib} + \varepsilon_{chem}) = \rho e - \rho \frac{u^2 + v^2}{2} + p \quad (3)$$

where h has been partitioned in translational, internal and chemical terms. The translational term is given by

$$h_{tr} = \bar{c}_p T = \alpha R^* T \quad (4)$$

where \bar{c}_p is the specific heat at constant pressure, $R^* = R/m$, R is the universal gas constant, and $m = \sum_s \chi_s m_s$ is the mean molar mass, being $\chi_s = m \rho_s / \rho m_s$ the molar fraction of the s th species. Internal temperature is not defined in state-to-state models, so that the internal contribution due to vibrational states is

$$\varepsilon_{vib} = \frac{1}{\rho} \sum_{s=1}^S \sum_{v=1}^{V_s} \rho_{s,v} \varepsilon_{s,v} \quad (5)$$

where $\varepsilon_{s,v}$ is the molecular energy density of the given vibrational level. The last term at the left hand side of Eq. (3) is the chemical contribution

$$\varepsilon_{chem} = \frac{1}{\rho} \sum_{s=1}^S \rho_s h_s^f \quad (6)$$

where h_s^f is the formation enthalpy per unit mass of component s . It should be pointed out that $\varepsilon_{s,v}$ and h_s^f are constants. In Eq. (4), the coefficient $\alpha = \sum_s \chi_s \alpha_s$ is the ratio between the specific heat due to degrees of freedom in equilibrium at the gas temperature T and R . In our case of diatomic molecules, considering equilibrium between rotation and translation, we have

$$\alpha_s = \begin{cases} 5/2 & \text{for monoatomic components} \\ 7/2 & \text{for biatomic components.} \end{cases}$$

Using the Mayer relation, $R^* = \bar{c}_p - \bar{c}_v$, where \bar{c}_v is the specific heat at constant volume, we define (see [27,28])

$$\bar{\gamma} \equiv \frac{\bar{c}_p}{\bar{c}_v} = \frac{\alpha}{\alpha - 1} \quad (7)$$

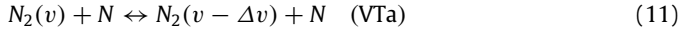
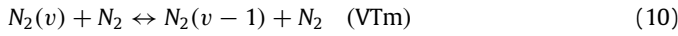
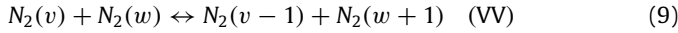
and, combining the state equation $p = \rho R^* T$ with Eq. (3), we get

$$p = (\bar{\gamma} - 1) \left[\rho e - \rho (\varepsilon_{vib} + \varepsilon_{chem}) - \rho \frac{u^2 + v^2}{2} \right]. \quad (8)$$

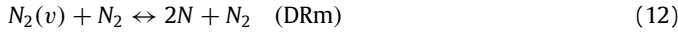
2.2. State-to-state kinetics

We consider a pure nitrogen mixture (N_2/N). The molar formation enthalpies are $H_{N_2}^f = 0$ and $H_N^f = 471036.3807$ J/mol. Only the ground state has been considered for atomic nitrogen, while

68 vibrational levels for N_2 , whose energies are given in [32]. The kinetic model is described in detail in [32,12] and includes two different kind of processes in the vibrational kinetics of pure nitrogen flows: internal energy exchange



and dissociation–recombination processes:



The rate coefficients of Eqs. (9)–(13) depend only on the gas temperature. The whole system consists of 69 species (68 for the N_2 vibrational levels and 1 for the atomic nitrogen N) which can interact through about 10000 elementary reactions. In the state-to-state model the vibrational temperature is not defined uniquely. Here we will consider the temperature of the first level

$$T_{Vs} = \frac{m_s(\varepsilon_{s,2} - \varepsilon_{s,1})}{k \ln \left(\frac{\rho_{s,1}}{\rho_{s,2}} \right)} \quad (14)$$

where k is the Boltzmann constant.

3. Numerical approach

The governing equation (1) is solved using an *operator splitting* approach [33] with two steps. The first one starts from $\mathbf{U}(t)$ and computes $\mathbf{U}^{\text{hom}}(t + \Delta t)$ imposing $\mathbf{W} = \mathbf{0}$, i.e., solves equation

$$\frac{\partial \mathbf{U}}{\partial t} + \frac{\partial \mathbf{F}(\mathbf{U})}{\partial x} + \frac{\partial \mathbf{G}(\mathbf{U})}{\partial y} = \mathbf{0} \quad (15)$$

whereas the second one evaluates $\mathbf{U}(t + \Delta t)$ from $\mathbf{U}^{\text{hom}}(t + \Delta t)$ neglecting the convective terms and solving the chemical equation locally, namely,

$$\frac{\partial \mathbf{U}}{\partial t} = \mathbf{W}(\mathbf{U}). \quad (16)$$

The homogeneous part is a 2D Euler equation for a non-reacting flow which is solved using the numerical scheme in [23], replacing the Roe's flux difference splitting solver with the Steger and Warming *flux vector splitting* [34] (for the implementation details see [35]) being the latter particularly suitable to solve flows with multicomponent mixture. The total energy flux component in the space discretization scheme has to be properly defined, see, e.g., [27,28].

In our operator splitting scheme, firstly Eq. (15) is advanced in time with step Δt , depending on the CFL condition (see [23]), by means of a second-order Runge–Kutta scheme, and then the inhomogeneous Eq. (16) is advanced using a sub-time step $\Delta t^{(v)}$, in order to account for the stiffness of source terms, such that

$$\sum_{v=0}^{n-1} \Delta t^{(v)} = \Delta t. \quad (17)$$

Depending on the case study, the sub-time step width may be fixed to $\Delta t^{(v)} = \Delta t/n$ or determined according to a suitable adaptive-step algorithm [36]. In this paper we have considered $n=4$ equally spaced subintervals.

The solution of Eq. (16) for the vector of partial densities $\mathbf{y} = \{\rho_i\}_{0 \leq i < N}$ changes only the partial densities of the chemical species and involves a matrix inversion whose solution has been carried out here with the following approach. We start rewriting Eq. (16) as

$$\frac{\partial \mathbf{y}}{\partial t} = \mathbf{P} - \mathbf{L} \cdot \mathbf{y} \quad (18)$$

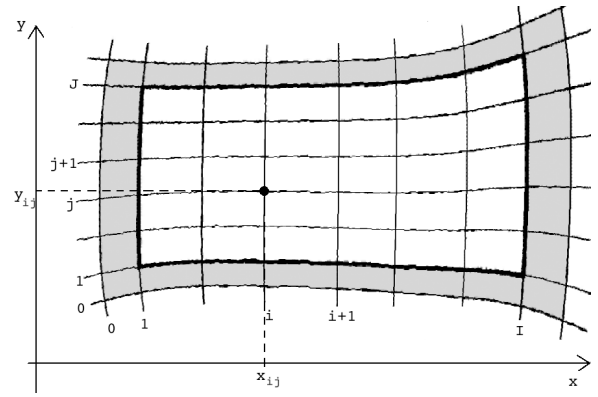


Fig. 1. General scheme of the structured two-dimensional grid with nodes reference, consisting of $I \times J$ grid points (nodes).

where \mathbf{P} is a vector and \mathbf{L} a diagonal matrix, The components P_i and $L_i y_i$ are nonnegative and represent, respectively, production and loss terms for component y_i . Considering a given time step $\Delta t^{(v)}$, the algorithm starts discretizing Eq. (18)

$$(\mathbf{I} + \Delta t^{(v)} \mathbf{L}) \cdot \mathbf{y}(t + \Delta t^{(v)}) = \Delta t^{(v)} \mathbf{P} + \mathbf{y}(t). \quad (19)$$

Although the system (19) has a linear form, it is not linear because \mathbf{L} and \mathbf{P} depend on \mathbf{y} . We use the Gauss–Seidel iterative scheme as

$$y_i \leftarrow \frac{\Delta t^{(v)} P_i(\mathbf{y}) + y_i}{1 + \Delta t^{(v)} L_i(\mathbf{y})}; \quad i = 0, \dots, N-1. \quad (20)$$

The parallelization of this problem is straightforward. We solve Eq. (20) for the same i in all the space. In this procedure each mesh point is assigned to a different thread, using the maximum capabilities of the GPU structure and reducing the memory occupancy. Moreover, the number of Gauss–Seidel iterations is kept constant in all the grid points, to avoid problems with thread synchronization and loss of efficiency. This aspect needs further investigation in order to optimize code performances.

3.1. Structured grids and domain decomposition

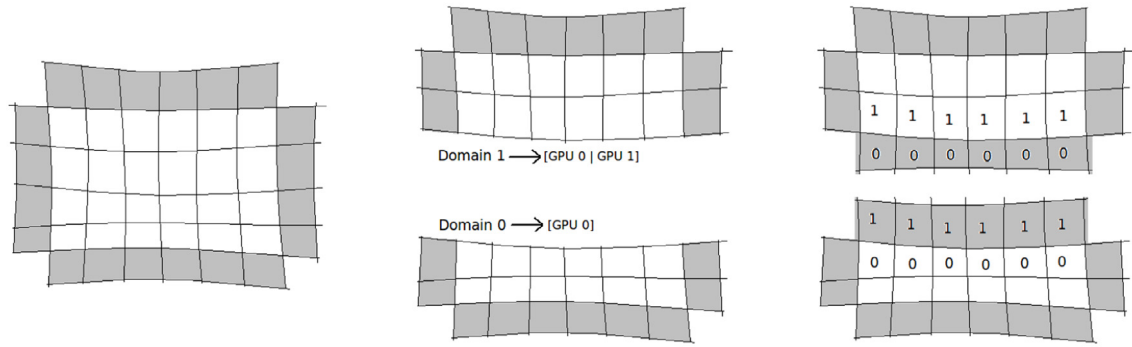
According to our previous work [23], we use a 2D structured grid, as drawn in Fig. 1 in the case of a single domain, where white cells cover the fluid domain and gray ones are *ghost cells* employed to impose the boundary conditions. The domain is discretized in the computational space using I nodes along the i direction and J nodes along the j direction.

In order to use multi-GPU architectures we have implemented a domain decomposition algorithm so that every sub-domain can be managed either by different GPUs or by the same GPU as well, in order to reduce the memory usage of the GPU. The algorithm is depicted in Fig. 2 where the use of the ghost cells to treat the boundary between sub-domains is highlighted. In this strategy, ghost cells are employed to evaluate the fluxes along a generic boundary edge: for an edge along the contour of the fluid domain, the values in the ghost cell are set so as to satisfy the boundary condition; whereas, for an internal edge, the ghost cells are represented by fluid cells of the adjacent sub-domain.

4. Nozzle flow

The first test case has been originally proposed to reproduce experimental results obtained in the EAST facility in NASA AMES [37], already investigated using state-to-state model in quasi-1D approximation [13] and recently also in 2D and 3D geometries [15]. This test case has been selected in order to assess

Non stair-stepped: $I_0 = I_1$



Stair-stepped: $I_0 \neq I_1$

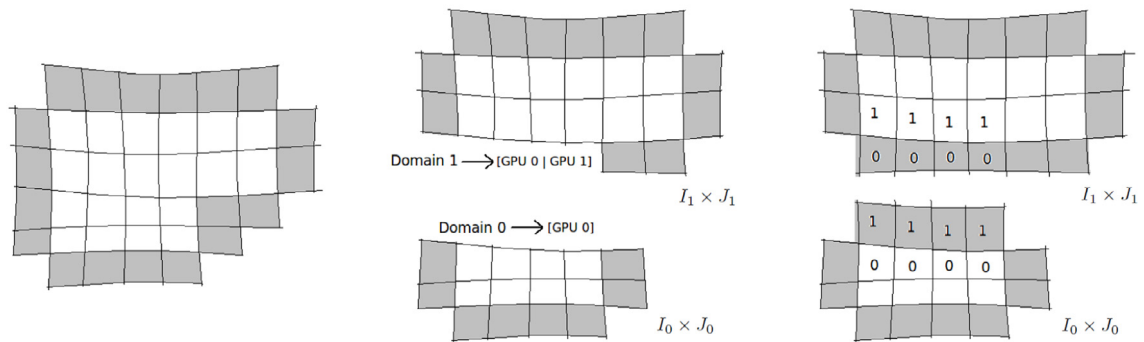


Fig. 2. Domain decomposition method: non stair-stepped and stair-stepped. White cells cover the fluid domain and gray ones are *ghost* cells employed to impose the boundary conditions.

the prediction capabilities of the state-to-state model in a simple 2D geometrical configuration, employing a single domain on a single GPU whose configuration is shown in Table A.1.

The EAST facility is a pulsed electric arc driven cylindrical shock tube expanding in a rectangular nozzle, resulting in stagnation conditions $T_0 = 5600$ K and $P_0 = 100$ atm. The experiment lasts for $175 \mu\text{s}$.

The nozzle throat is 0.64 cm high and 8.3 cm wide and therefore a 2D model is adequate. The nozzle section A can be described by the following expression:

$$\frac{A}{A_t} = 1 + \left(\frac{x}{2.54} \right)^2 \quad (21)$$

where A_t is the section at the throat and x , expressed in cm, is the position along the nozzle axis relative to the throat. The area at the exit section ($x_e = 8$ cm) is $A_e \approx 11A_t$.

4.1. Computational details

The flow has been computed on a structured grid representing half-nozzle (see Fig. 3), consisting of 65×47 fluid cells ($I = 66$, $J = 48$). The mesh was built in such a way that the equally spaced i -lines are almost perpendicular to the equally spaced j -lines (quasi-conformal grid).

Boundary conditions have been imposed according to the theory of characteristics: subsonic condition at the inflow points ($i = 1$), supersonic condition at the outflow points ($i = I$), symmetry at the lower boundary ($j = 1$) and inviscid wall at the upper boundaries ($j = J$). Initial conditions are summarized in Table 1.

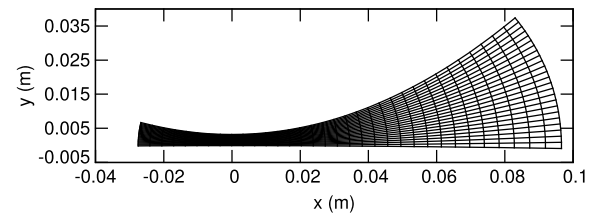


Fig. 3. Grid scheme of the 2D Sharma nozzle: 65×47 fluid cells ($I = 66$, $J = 48$).

Table 1

Initial conditions in Sharma nozzle simulation.

	Before throat	After throat
P	$P_0 = 100$ atm	0.197 atm
T	$T_0 = 5600$ K	300 K
(u, v)	$(0, 0)$	$(0, 0)$
N_2 molar fraction ^a	0.9828	1
$N_2(v)$ distribution	Boltzmann at T_0	Boltzmann at 300 K
N molar fraction ^a	0.0172	$1.12923\text{e}-79$

^a Equilibrium calculation.

4.2. Comparison with experimental data

In order to verify the extent of thermodynamic non-equilibrium during the fast transient and at steady-state, a time accurate integration has been carried out. Results have been reported along the nozzle axis focusing on points where experimental distributions have been measured [37], namely, $x_0 = -0.6$, $x_1 = 2.4$, $x_2 = 5.4$, $x_3 = 8.0$.

The N_2 vibrational distributions along the nozzle axis ($j = 1$) are provided in Fig. 4. Non-Boltzmann trend of vibrational distributions is observed during the transient and at stationarity,

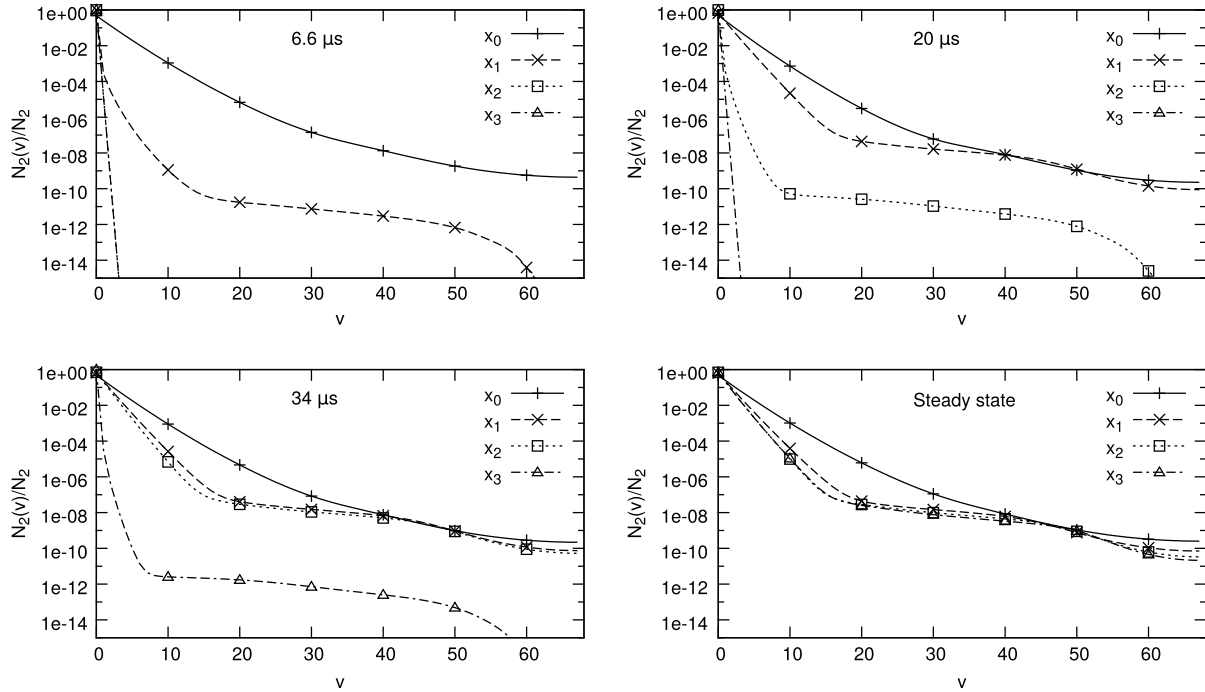


Fig. 4. Time evolution, up to steady state, of the N_2 vibrational distributions at different points along the nozzle axis.

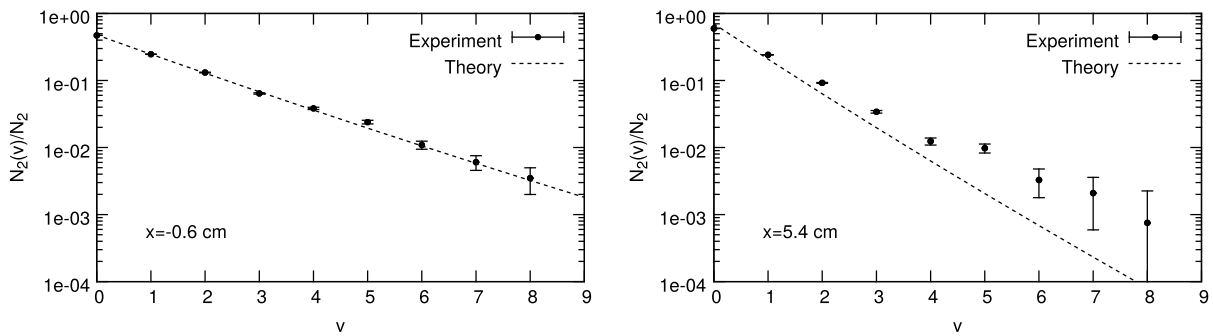


Fig. 5. Comparison between experimental [37] and calculated distributions at steady state at two points along the nozzle axis.

confirming the need of the state-to-state approach in supersonic nozzle expansion. Non-equilibrium is observed in the expanding region, where long plateaux due to atomic recombination appears. The comparison with experimental data limited to $v \leq 8$ [37] at steady state, is given in Fig. 5, showing a satisfactory agreement.

Concerning the behavior in the cross section, the distributions are very similar in points x_1 , x_2 and x_3 , while during the evolution non uniform behavior has been observed.

The time evolutions of various macroscopic quantities have been calculated, all showing a perturbation wave which can be observed while crossing the nozzle, until the stationary state has been reached, obtained after 80 μ s.

As an example, Fig. 6 reports the time evolution along the nozzle axis of vibrational and translational temperatures. The stationary profile has been compared with the experimental values taken from Ref. [37], showing good prediction capability.

These results are in line with those reported in the literature [13,15].

4.3. Reacting flow computational performance

The *Total* execution time of our numerical model implementation, thanks to the operator splitting scheme, can be divided into an *Advection* execution time, related to the computation of the

homogeneous equation (see Eq. (15)), and a reactive *Kinetics* execution time, related to the computation of the master equation (see Eq. (16)), so that

$$Total = Advection + Kinetics.$$

The values of the *Total* execution time of the simulation described in Section 4.2 are plotted, as a function of the advection time steps, in Fig. 7(Left) for both the CPU and the GPU version of the code, showing the same linear trend but with a constant ratio CPU/GPU of about two orders of magnitude.

It is noteworthy that the ratio *Kinetics/Total* shows that the whole execution time is almost all spent for the kinetics computation, 95% in the GPU version and about 100% in the CPU one.

The speed-up CPU/GPU is plotted in Fig. 7(Right) separately for the *Total* and the *Kinetics* execution times. In both cases a value of above 100 is reached in the first few time steps and remains constant until the rest of the computation.

5. Flow past a circular cylinder

The second test case is relative to the formation of a bow shock in front of a blunt body in high enthalpy flows. Differently from the nozzle flow investigated in the previous section, the free

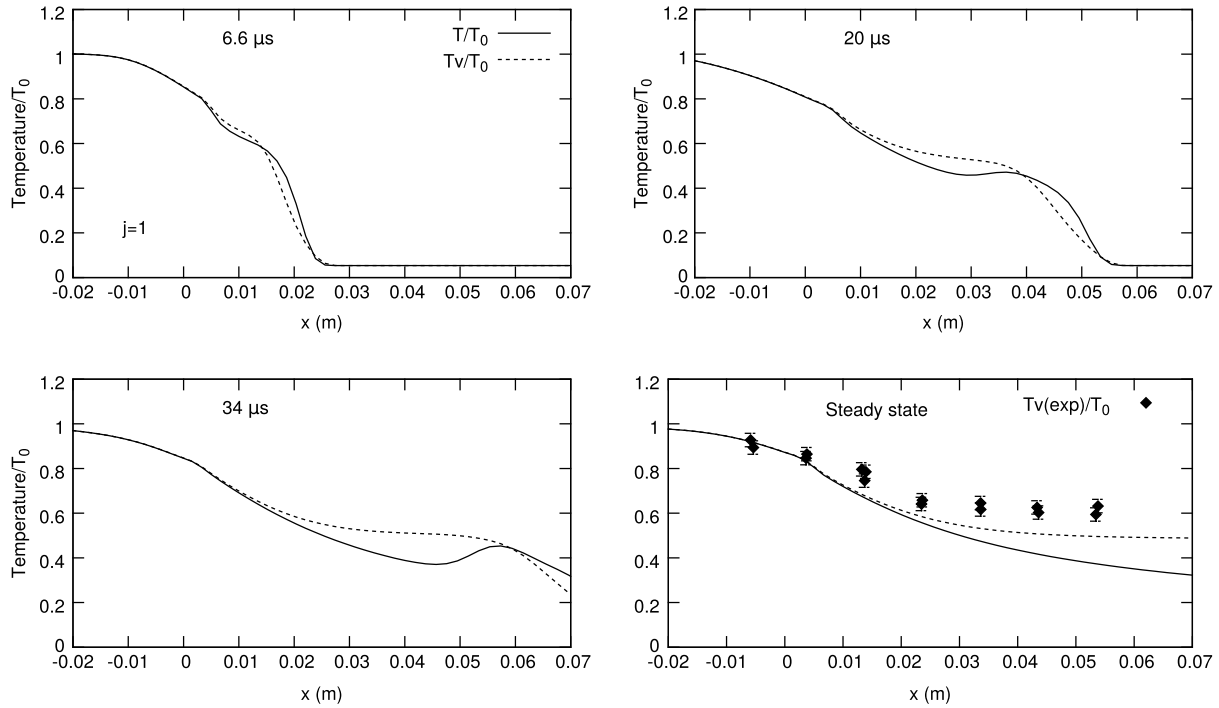


Fig. 6. Time evolution, up to stationarity, of T/T_0 (solid line) and T_v/T_0 (dashed line) along the nozzle axis. The stationary values are compared with experimental data in Ref. [37].

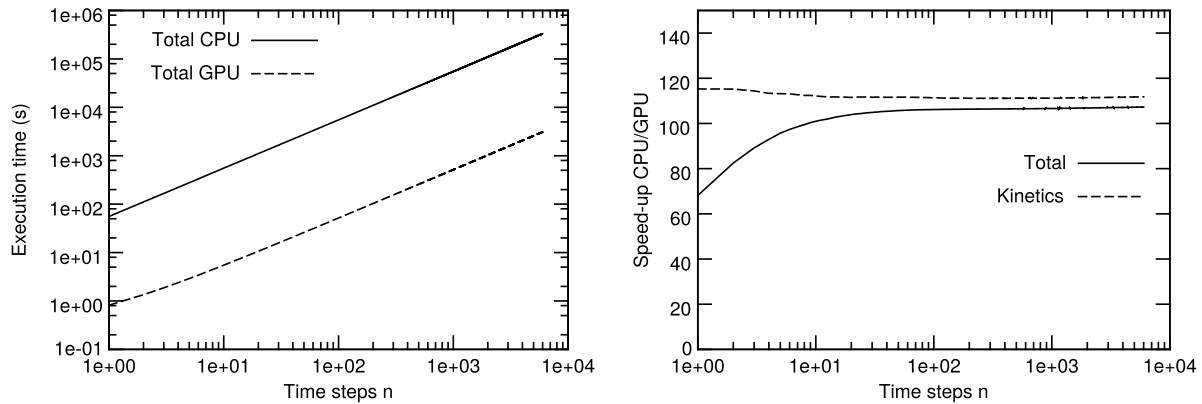


Fig. 7. Execution time versus advection time steps of the simulation described in Section 4.2. Left: Total execution time of the serial (CPU) version of the code (solid line) and of the parallel (GPU) version (dashed line); Right: Speed-up CPU/GPU of the Total execution time (solid line) and of the Kinetics execution time (dashed line).

flow gas is composed of molecules only, at very low temperature, and the evolution of the distribution is observed past the shock front, where the vibrational distribution increases the temperature activating dissociation.

The flow configuration presents a high free-stream Mach number, so that a strong steady bow shock wave will form in front of the cylinder. Just behind the shock front the gas temperature increases rapidly at very high values, while the vibration temperature and the gas composition maintain the same values as in the free flow. As a consequence, collisions heat the vibrational distributions and the dissociation of molecule starts; thus, the gas temperature decreases, transferring energy to internal degrees of freedom and to chemical processes. The relaxation time of these different processes affects the stand-off distance as well as the heat flux to the surface.

5.1. Computational details and results

The computational domain has been decomposed into four sub-domains plotted in Fig. 8, using the approach schematized in Fig. 2, under the boundary conditions described below.

$$\begin{aligned}
 I_d \times J_d &= 154 \times 23, \quad d = 0, 1, 2, 3 \\
 i = 1: & \text{Supersonic inlet, } p_\infty = 2910 \text{ Pa,} \\
 & T_\infty = 1833 \text{ K} \\
 i = I_d: & \text{Inviscid wall (cylinder border)} \\
 j = 1: & \begin{cases} \text{Symmetry condition} & d = 0 \\ \text{Interdomain boundary} & d = 1, 2, 3 \end{cases} \\
 j = J_d: & \begin{cases} \text{Interdomain boundary} & d = 0, 1, 2 \\ \text{Supersonic outlet} & d = 3. \end{cases}
 \end{aligned}$$

The calculations were carried out through the single-GPU system whose configuration is shown in Table A.2. All the domains are managed by the same GPU.

For validation purposes, flow conditions have been taken from the classical work of Hornung [38], comparing our results with calculations in similar conditions [39,40]. Experiments were performed [38] for a cylinder with radius $R = 1/2$ inch, with the free-stream gas composed of nitrogen partially dissociated with initial conditions summarized in Table 2. The steady-state configuration has been reached after $50 \mu\text{s}$ by the time accurate simulation.

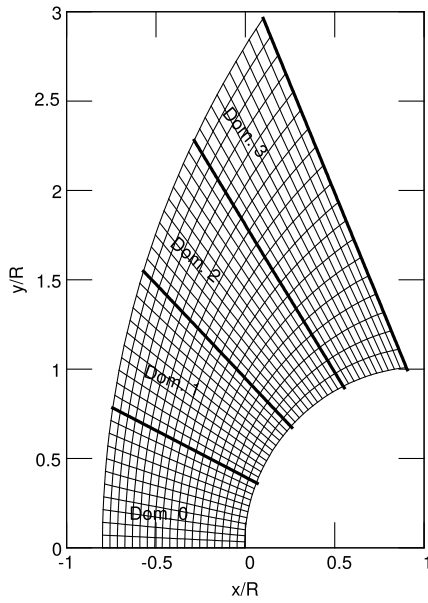


Fig. 8. 2D domain decomposition scheme around a circular cylinder, radius $R = 1.27$ cm (half-inch), $l_d \times J_d = 154 \times 23$, $d = 0, 1, 2, 3$.

Table 2

Initial conditions for the flow past a circular cylinder in Fig. 8.

	Inlet ($i = 0, -1$) ghost cells	All fluid cells
p	$p_\infty = 2910$ Pa	p_∞
T	$T_\infty = 1833$ K	T_∞
Mach	$M_\infty = 6.14$	0
(u, v)	(5590 m/s, 0)	(0, 0)
N_2 mass fraction	0.927	0.927
$N_2(v)$ distribution	Boltzmann at T_∞	Boltzmann at T_∞
N mass fraction	0.073	0.073
$[N_2]$ mol/m ³	$[N_2]_\infty = 0.16496$	$[N_2]_\infty$
$[N]$ mol/m ³	$[N]_\infty = 0.02598$	$[N]_\infty$

In order to validate the code with available results [38, p. 165] we have also considered the case with frozen flow, i.e., neglecting the contribution of chemical reactions. The computed density profiles along the stagnation streamline, for the frozen and reactive non-equilibrium cases, given in Fig. 9, are consistent with those reported by Hornung [38, p. 159]. In the case of frozen flow, we have obtained a stand-off distance $\Delta/R = 0.466$, associated with the ratio $\rho_\infty/\rho_s = 0.194$ (the subscript 's' indicating, hereafter, the quantities immediately behind the normal shock), that is in very good agreement with the results of Lomax and Inouye [38, p. 165], which report a value $\Delta/R = 0.45$.

An important quantity to correlate the stand-off distance with the flow pattern of non-equilibrium dissociating flow of nitrogen is the so called “normal shock reaction rate parameter”, defined as [38, eq. 24]:

$$\Omega = \left(\frac{dw_N}{dt} \right)_s \frac{R}{u_\infty} \quad (22)$$

where w_N is the atomic nitrogen mass fraction and $\left(\frac{dw_N}{dt} \right)_s$ is the nitrogen reaction rate immediately behind the normal shock. We have calculated Ω following the state-to-state kinetics described in Section 2.2.

The reaction rate of the molar densities $[N_2(v)]$ and $[N]$ due to dissociation and recombination processes are

$$\begin{aligned} \frac{d[N_2(v)]}{dt} = & -k_m^d(v)[N_2(v)][N_2] - k_a^d(v)[N_2(v)][N] \\ & + k_m^r(v)[N]^2[N_2] + k_a^r(v)[N]^3 \end{aligned} \quad (23)$$

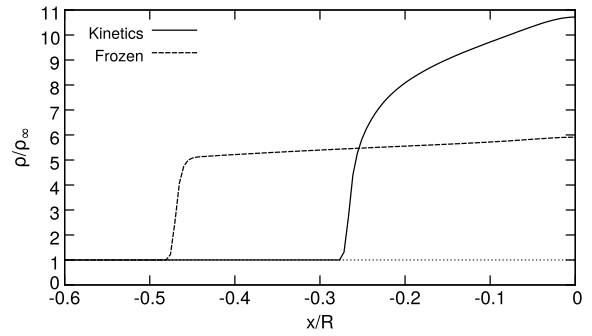


Fig. 9. Density profile along the stagnation streamline at steady state: frozen flow and reactive non-equilibrium (kinetics) flow.

$$\frac{d[N]}{dt} = -2 \sum_v \frac{d[N_2(v)]}{dt} \quad (24)$$

where $k_m^d(v)$ is the rate coefficient for the dissociation of N_2 molecule in the v th vibrational state by collisions with molecules, see Eq. (12), and $k_m^r(v)$ the rate of the reverse process, while $k_a^d(v)$ and $k_a^r(v)$ are the corresponding processes by atom collisions, see Eq. (13).

According to our scheme, namely Eq. (18), the global atomic nitrogen reaction rate, directly arising from Eq. (24), is given as:

$$\frac{dw_N}{dt} = \left(\frac{dw_N}{dt} \right)_m^+ + \left(\frac{dw_N}{dt} \right)_a^+ - \left(\frac{dw_N}{dt} \right)_m^- - \left(\frac{dw_N}{dt} \right)_a^- \quad (25)$$

where the four contributions (partial reaction rates) have the following detailed expressions:

$$\left(\frac{dw_N}{dt} \right)_m^+ = \frac{1}{m_{N_2}} \sum_v k_m^d(v) w_{N_2(v)} w_{N_2} \quad (26)$$

$$\left(\frac{dw_N}{dt} \right)_m^- = \frac{\rho^2}{m_N^2} \sum_v k_m^r(v) w_N^2 w_{N_2} \quad (27)$$

$$\left(\frac{dw_N}{dt} \right)_a^+ = \frac{\rho}{m_N} \sum_v k_a^d(v) w_{N_2(v)} w_N \quad (28)$$

$$\left(\frac{dw_N}{dt} \right)_a^- = \frac{2\rho^2}{m_N^2} \sum_v k_a^r(v) w_N^3 \quad (29)$$

where m_{N_2} and m_N are the molar mass of the molecular and atomic nitrogen respectively.

The above quantities have been calculated along the stagnation streamline and reported, at steady state, in Fig. 10. As expected, both positive contributions (dissociations by atoms and molecules) are dominant behind the shock front, while negative terms (recombinations) are orders of magnitude smaller. Approaching the cylinder wall, the atomic density increases and, as a consequence, the negative terms grow while the positive ones diminish, going towards the limit of equal values of positive and negative contributions, obtained in case of local thermodynamic equilibrium.

The dimensionless atomic nitrogen reaction rate $\frac{dw_N}{dt} \frac{R}{u_\infty}$ and ρ/ρ_∞ are reported in Fig. 11. The aforesaid reaction rate shows a sharp peak just after the shock front, rapidly decreasing for the dissociation. On the other hand, the density profile grows regularly, because, due to dissociation the temperature decreases and, following the Le Chatelier principle, the density should increase to compensate the pressure drop. The parameter Ω is calculated at the maximum of $\frac{dw_N}{dt} \frac{R}{u_\infty}$, immediately behind the normal shock, obtaining $\Omega = 0.97$, corresponding to $\rho_s/\rho_\infty = 5.83$. We have estimated the stand-off distance as $\Delta/R = 0.27$ (see Fig. 9) and

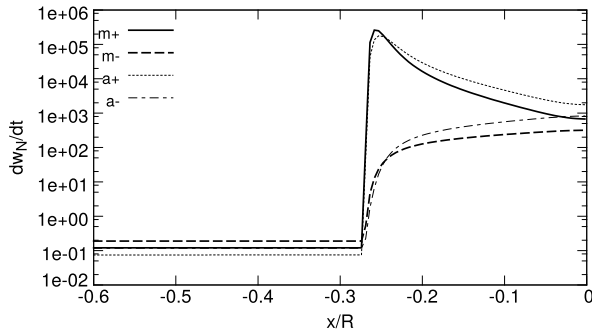


Fig. 10. Profile along the stagnation streamline of the atomic nitrogen reaction rate partial contributions; $a+ = \left(\frac{dw_N}{dt}\right)_a^+$, $a- = \left(\frac{dw_N}{dt}\right)_a^-$, $m+ = \left(\frac{dw_N}{dt}\right)_m^+$, $m- = \left(\frac{dw_N}{dt}\right)_m^-$.

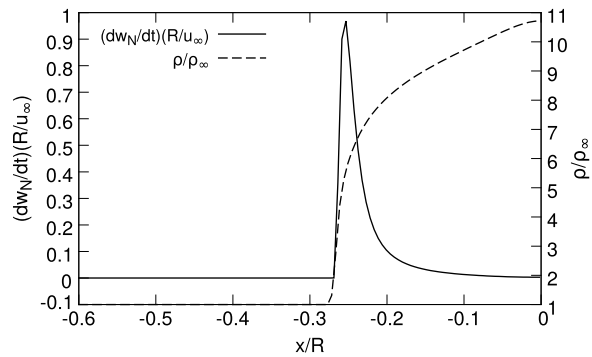
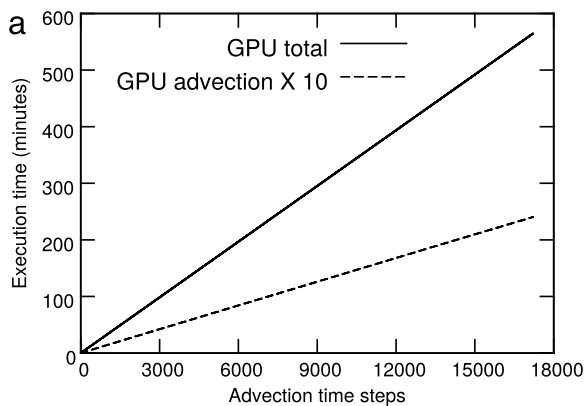


Fig. 11. Dimensionless atomic nitrogen reaction rate $\left(\frac{dw_N}{dt}\right) \cdot \left(\frac{R}{u_\infty}\right)$ and ρ/ρ_∞ , calculated along the stagnation streamline.

then the quantity $\frac{1}{2}(\Delta/R)(\rho_s/\rho_\infty) = 0.79$, which is associated with $\Omega = 0.97$. The correlation between these two quantities is in excellent agreement with the calculation of Garr and Marrone [38, Fig. 10, p. 165].

The GPU execution times for the test described in this section are summarized in Fig. 12. The ratio of the total execution time over the execution time spent only for the advection steps has an asymptotic constant value of 23, which is very rapidly reached after the first 100 time steps. This transient behavior is due to the initialization procedure, that is included in the determination of computational time. In this test case, similarly to what has been noticed for the first test case discussed in Section 4, the execution time spent to solve the kinetics step is about the 96% of the total execution time.



In order to better analyze the scaling performance of the proposed GPU approach, we have repeated the simulations of this test case using a more recent single-device, belonging to the system shown in Table A.3. Moreover, two grids have been employed: (1) the grid previously described, see Fig. 8, and referred to as Grid 1; (2) a finer grid, named Grid 2, having twice the number of cells in the j -direction; thus, for each subdomain, $J_d \rightarrow 2J_d - 1$ and the mesh has twice the number of cells of Grid 1. For both grids, Fig. 13 provides the GPU execution time obtained over the advection time steps for a (real) time interval of $50 \mu s$ (broken lines). It appears that the finer mesh requires just 25% more GPU time to complete the simulation, thus almost doubling the efficiency in terms of speed-up t_{CPU}/t_{GPU} , as shown in Fig. 14.

6. Blunt body in hypersonic wind tunnel

An interesting test case is to model a realistic system, i.e. a blunt body in a hypersonic wind tunnel. For sake of completeness, we have adapted the nozzle used in Section 4.2 considering a cylinder at the nozzle exit.

The nozzle, with a rectangular cross section given by the following quadratic profile (slightly different from that in Eq. (21))

$$\frac{A}{A_t} = 1 + \left(\frac{x}{2.143}\right)^2 \quad (30)$$

has a throat height of 0.64 cm and is 8.3 cm long, where A_t is the throat section and x , measured in cm, is the distance from the throat. It follows that the expansion coefficient is $A_{exit}/A_{throat} = 16$. Also in this case we have divided the computational grid in four domains, as schematized in Fig. 15, conformally deformed to fit the cylinder surface, having radius $R = 0.8263$ cm, whose center is placed on the nozzle axis at $x_c = 10.64$ cm from the throat.

Initial conditions are summarized in Table 4. The calculation was carried out through the two-GPU system whose configuration is shown in Table A.1; more precisely: Device-0 manages Domain-0 and Domain-1, Device-1 manages Domain-2 and Domain-3.

6.1. Reacting flow simulations

The calculations are intended to mimic the behavior of hypersonic ground test facility in the nozzle-obstacle configuration. The presence of the obstacle perturbs the flow field and a shock wave is formed in front of the cylinder, with the consequent increase of pressure, temperature and density, while the speed is reduced to subsonic values. Differently from the case discussed in Section 5, the distributions of the molecules crossing the shock front are already out of equilibrium, as well as the composition, corresponding approximately to the conditions met at the nozzle exit.

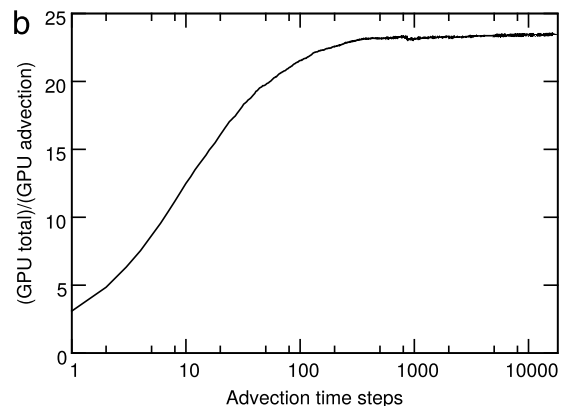


Fig. 12. GPU execution times as a function of the advection time steps: (a) total (solid line) and advection times ten (dashed line); (b) ratio (total)/(advection).

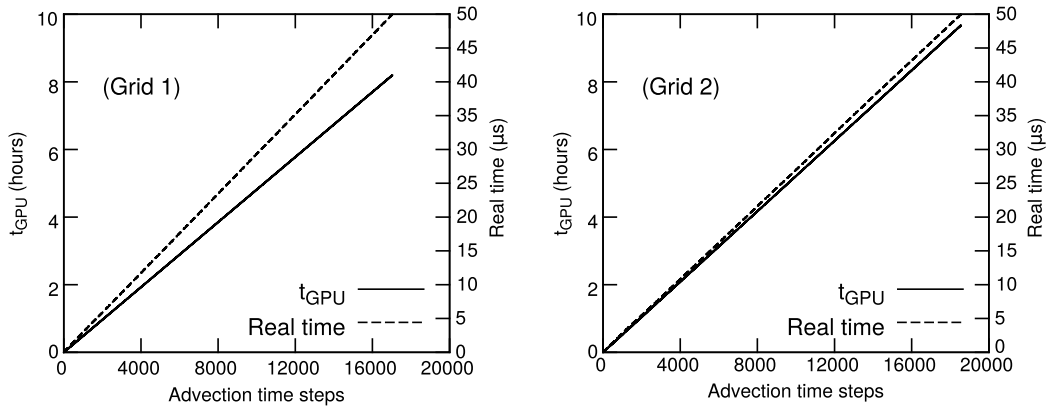


Fig. 13. GPU execution time and real time as a function of the advection time steps, for the Grid 1 (Left) and the Grid 2 (Right): simulation performed by a single-GPU belonging to the system shown in Table A.3.

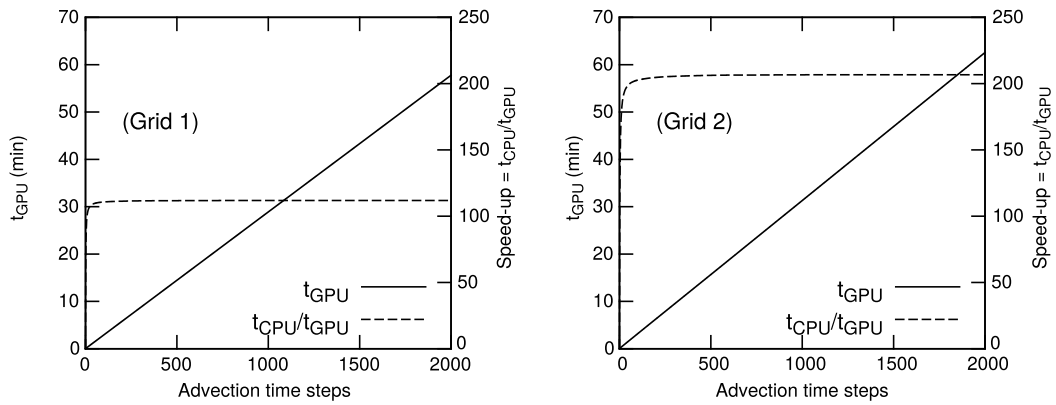


Fig. 14. GPU execution time t_{GPU} and speed-up t_{CPU}/t_{GPU} as a function of the advection time steps, for the Grid 1 (Left) and the Grid 2 (Right): simulation performed by a single-GPU and a single CPU belonging to the system shown in Table A.3.

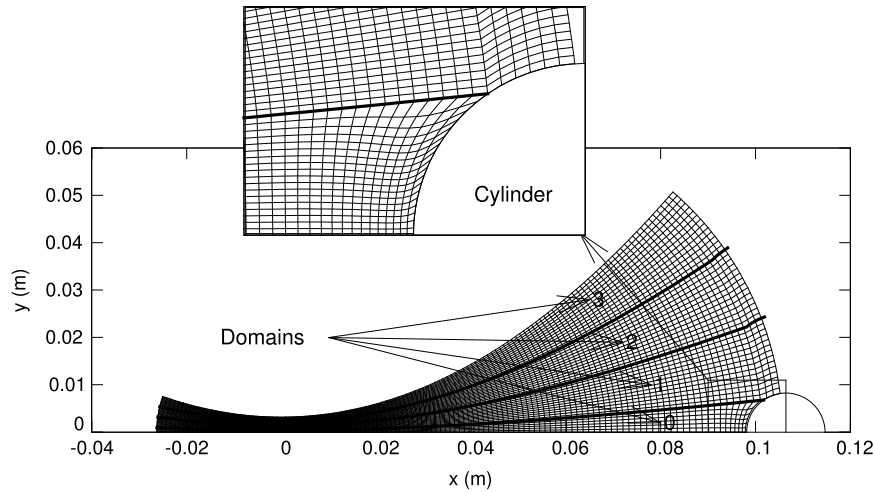


Fig. 15. Circular cylinder in the divergent part of a 2D nozzle. Subdomain grids are given in Table 3.

Starting from the initial conditions described in Table 4, steady state has been reached after $137 \mu\text{s}$. Fig. 16 shows the time evolution, up to $t = 87.5 \mu\text{s}$ of the reduced translational temperature T/T_0 and the N_2 vibrational distributions in four fixed points D_1, \dots, D_4 (see Table 5 for the corresponding coordinates), along the border line between Domain-1 and Domain-2. The relative steady solution is reported in Fig. 17. After $37 \mu\text{s}$ the flow has not yet reached the obstacle, as indicated by the position of the shock that separates the flow and the gas at rest. Point D_4 is in the cold region and therefore the vibrational distribution is not developed

yet. Two types of distributions can be observed, depending on the conditions: if recombination is dominating the distribution shows a plateau, as in the nozzle expansion described in Section 4, with a characteristic S shape, while in case of dissociation regime it follows a Boltzmann trend for low v with depleted high energy levels, showing a wedge shape. It should be noted that, during the evolution, in each point the distributions pass different phases, alternating recombination and dissociation regimes, following the local temperature and pressures, determined by the passage of the flow front. In any cases the distributions are non-Boltzmann. At steady

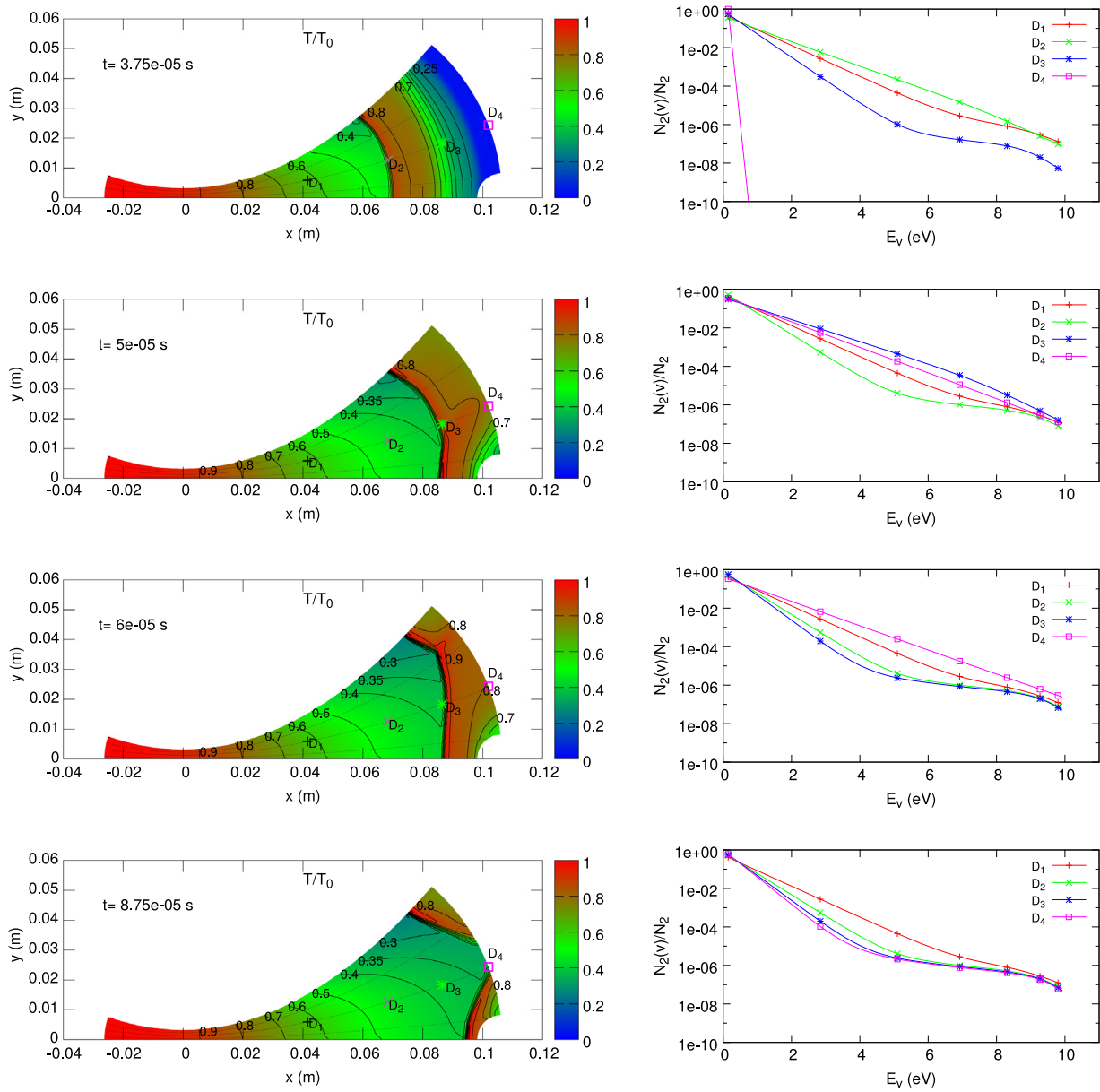


Fig. 16. Time evolution up to $t = 87.5 \mu\text{s}$ of the translational temperature T , in unit of the stagnation temperature $T_0 = 10000 \text{ K}$, and the N_2 vibrational distributions, as mass fractions $\rho_{N_2(v)} / \sum_v \rho_{N_2(v)}$, $v = 0, \dots, 68$, in the fixed points D_1, \dots, D_4 , given in Table 5.

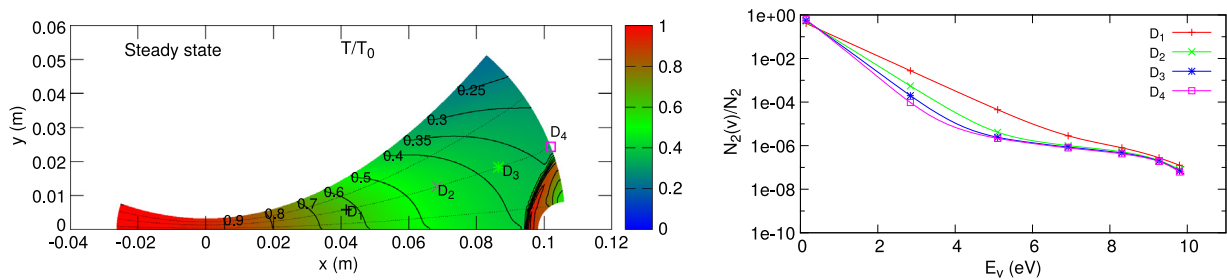


Fig. 17. Reduced translational temperature 2D map and the corresponding N_2 vibrational distributions in the fixed points D_1, \dots, D_4 given in Table 5.

state, the points are all in the expansion zone, outside the shock, and therefore the distributions reproduce the same characteristics already observed for the nozzle flow.

The comparison between translational and vibrational reduced temperatures at steady state is shown in Fig. 18. In the expanding

region just after the throat the two temperatures are practically equal, but close to the exit, corresponding to $T/T_0 < 0.4$, the two temperatures show different behaviors. Moreover, Fig. 19 provides N_2 vibrational distributions at steady state in points depicted in Fig. 18 and given in Table 6.

Table 3

Dimension and boundary conditions of the subdomains plotted in Fig. 15.

Domain 0: $I_0 \times J_0 = 248 \times 19$
$i = 1$: Subsonic inlet, $p_t = 83.33$ bar, $T_t = 10000$ K
$i = I_0$: Inviscid wall (cylinder border)
$j = 1$: Symmetry conditions
$j = J_0$: Interdomain boundary
Domain 1: $I_1 \times J_1 = 254 \times 43$
$i = 1$: Subsonic inlet, $p_t = 83.33$ bar, $T_t = 10000$ K
$i = I_1$: Supersonic outlet
$j = 1, i \leq 248$: Interdomain boundary
$j = 1, i > 248$: Inviscid wall (cylinder border)
$j = J_1$: Interdomain boundary
Domain 2: $I_2 \times J_2 = 254 \times 43$
$i = 1$: Subsonic inlet, $p_t = 83.33$ bar, $T_t = 10000$ K
$i = I_2$: Supersonic outlet
$j = 1$: Interdomain boundary
$j = J_2$: Interdomain boundary
Domain 3: $I_3 \times J_3 = 254 \times 43$
$i = 1$: Subsonic inlet, $p_t = 83.33$ bar, $T_t = 10000$ K
$i = I_3$: Supersonic outlet
$j = 1$: Interdomain boundary
$j = J_3$: Inviscid wall (nozzle border)

Table 4

Initial conditions for the flow through the 2D nozzle in Fig. 15.

	Before throat	After throat
p	$p_0 = 83.33$ bar	0.197 bar
T	$T_0 = 10000$ K	300 K
(u, v)	(0, 0)	(0, 0)
N_2 molar fraction ^a	0.12	1
$N_2(v)$ distribution	Boltzmann at T_0	Boltzmann at 300 K
N molar fraction ^a	0.88	$1.12923e-79$

^a Equilibrium calculation.**Table 5**Points along the boundary: domain = 1, $j = 43$.

Point	i	x (cm)	y (cm)
D_1	150	4.18	0.60
D_2	200	6.83	1.30
D_3	230	8.64	1.78
D_4	254	10.2	2.44

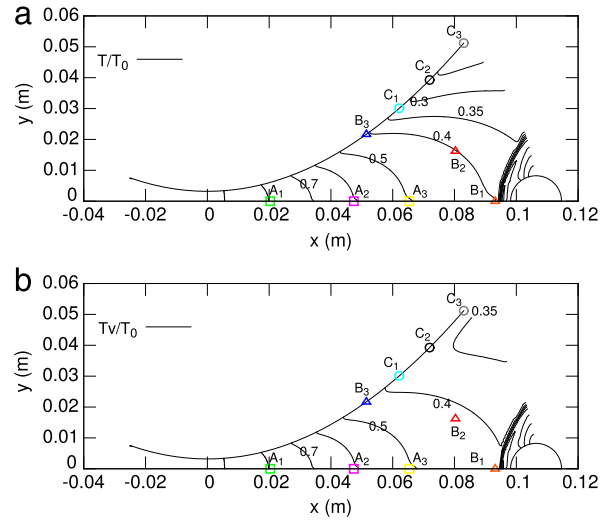
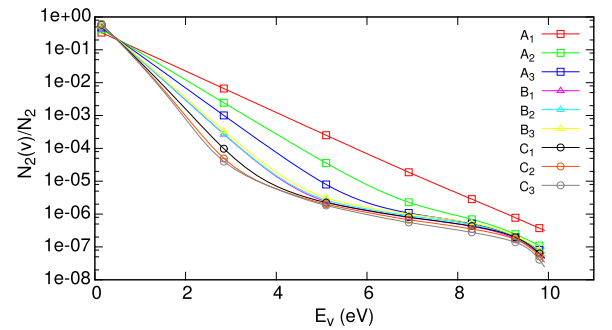
Table 6

Points in Figs. 18 and 19.

Point	(dom, i, j)	x (cm)	y (cm)
A_1	(0, 105, 1)	2.04	0.00
A_2	(0, 160, 1)	4.75	0.00
A_3	(0, 192, 1)	6.60	0.00
B_1	(0, 236, 1)	9.33	0.00
B_2	(1, 220, 43)	8.07	1.60
B_3	(3, 180, 43)	5.15	2.17
C_1	(3, 205, 43)	6.22	3.01
C_2	(3, 228, 43)	7.19	3.89
C_3	(3, 254, 43)	8.29	5.11

All the chosen points are outside the shock layer. In points $A_1 - A_3$ and B_1 , placed along the nozzle axis, the distributions vary from an equilibrium profile toward a typical supersonic non-equilibrium one moving toward the nozzle exit. In points B , placed along the translational temperature isoline 0.4, the distributions do not change, while small variations are observed in the distributions between points C , placed along the nozzle wall.

Fig. 20 shows the reduced temperature map in the region close to the obstacle. A small region in which $T/T_0 \approx 1$ can be observed around the normal shock. Four sampling points are considered along the cylinder surface, from $\theta = 0$, corresponding to the stagnation point, S_1 , to $\theta = \pi/2$. In points S_1 and S_2 the vibrational and translational temperatures are equal and the same is observed

**Fig. 18.** Reduced translational T (a) and vibrational T_v (b) temperatures at steady state.**Fig. 19.** N_2 vibrational distributions in the points reported in Table 6 and marked in Fig. 18.**Table 7**Points along the stagnation streamline ($j = 1$).

Point	i	x/R
P_1	238	-0.473
P_2	239	-0.413
P_3	240	-0.357
P_4	241	-0.303
P_5	248	0.000

for the distributions, demonstrating local thermal equilibrium in this region of the surface. In S_3 and S_4 there is again an expansion zone, so that $T < T_v$, and the vibrational distributions show the characteristic shape met in recombination regimes.

Let us now analyze the evolution of the distribution inside the shock. At this purpose we have considered five sampling points along the nozzle axis: from P_1 , just before the shock, up to P_5 , the stagnation point, see Table 7 for coordinates. The distributions sampled in the P_i points are shown in Fig. 21, while the profiles of T and T_v along the nozzle axis are shown in Fig. 22.

Fig. 23 shows the time evolution of the N mass fraction and the translational temperature in the stagnation point on the cylinder surface. As the flow reaches the surface, the temperature rapidly increases, activating the dissociation of molecules, that is faster than the flow characteristic time, therefore a minimum in the temperature appears. After the minimum, the flow impinging the surface is already dissociated and as a consequence, temperature and atomic molar fraction grow up to an equilibrium value.

Fig. 24 provides the mass fraction of N atoms (c_N) at $t = 50 \mu s$ and at steady state. At $t = 50 \mu s$ we can observe that the recombination is effectively reducing N mass fraction at 0.7 in the

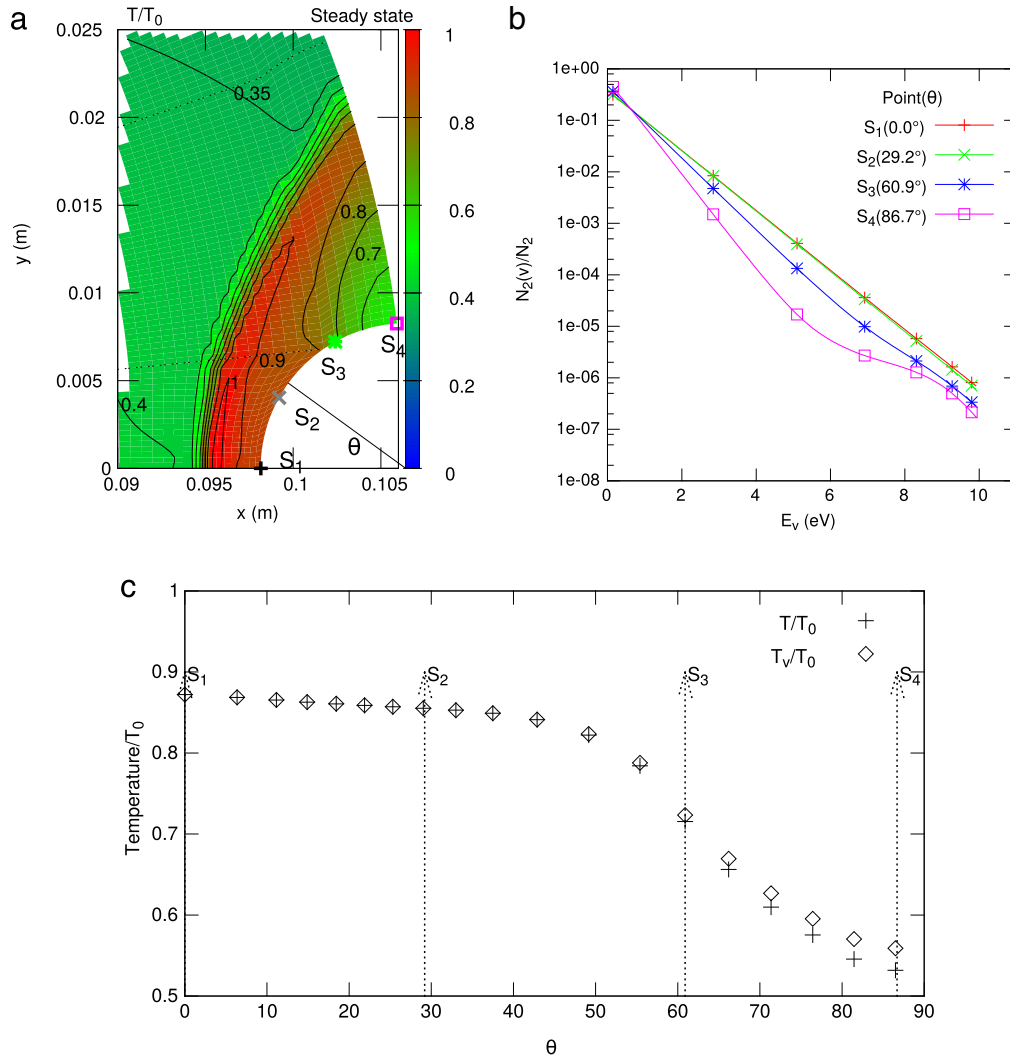


Fig. 20. (a) Contours of the translational temperature T , in unit of the stagnation temperature $T_0 = 10,000$ K; (b) N_2 vibrational distributions, as mass fractions $\rho_{N_2(v)}/\sum_v \rho_{N_2(v)}$, $v = 0, \dots, 68$, in the fixed points S_1, \dots, S_4 on the cylinder surface; (c) T and T_v 1D-profile along the cylinder surface.

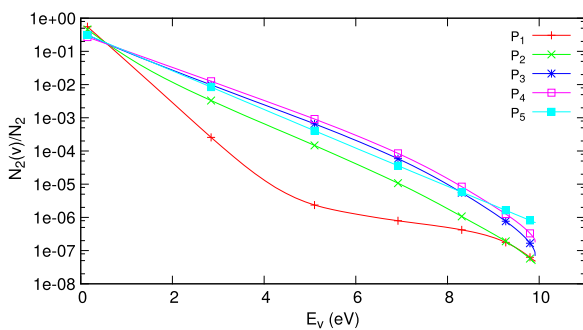


Fig. 21. N_2 vibrational distributions, as mass fractions $\rho_{N_2(v)}/\sum_v \rho_{N_2(v)}$, $v = 0, \dots, 68$, in the points P_1, \dots, P_5 , given in Table 7, along the nozzle axis and through the bow shock.

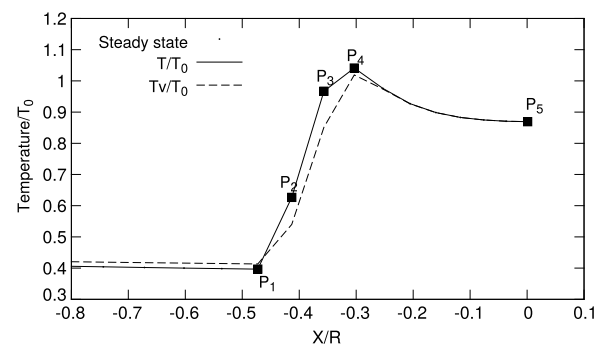


Fig. 22. Translational T and vibrational T_v temperatures, in unit of the stagnation temperature $T_0 = 10,000$ K, along the nozzle axis, as a function of the distance from the cylinder surface, in unit of the cylinder radius.

throat. The recombination process is appreciable also in the diverging section of the nozzle, reaching a minimum in the central zone, where $c_N \approx 0.55$. It is possible to observe also a dissociation region, covering the whole section, created by the perturbation of the blunt body. Close to the body surface, the gas is formed mainly by molecules, because the shock layer still contains the originally

cold gas and the compression was not capable to initiate the dissociation. A maximum can also be observed in the front of the shock wave, where $c_N \approx 0.7$. At steady state this complex structure disappears. In the diverging part the molar fraction varies very weakly, while at the nozzle exit, far from the body, the free flow condition is observed. Close to the blunt body, we can see a hot

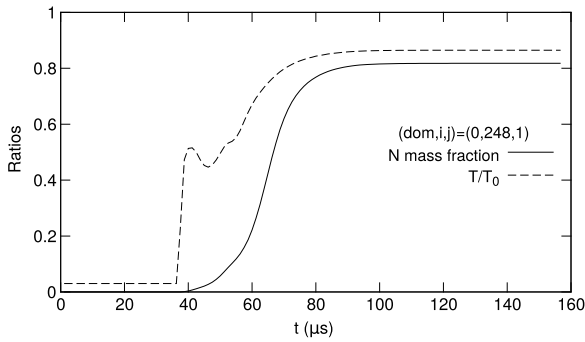


Fig. 23. Time evolution of the N mass fraction and the ratio T/T_0 in the stagnation point $(dom, i, j) = (0, 248, 1)$ on the cylinder surface.

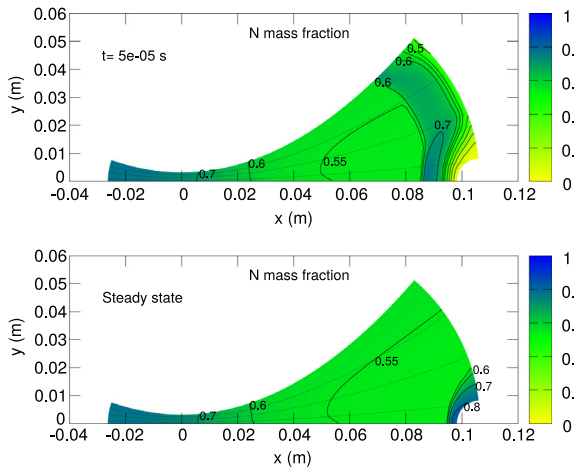


Fig. 24. N mass fraction at $t = 50 \mu s$ (upper plot) and at stationarity (lower plot).

shock wave, where the atom mass fraction reaches its maximum for $c_N \approx 0.8$ at the surface.

The general trends of the GPU execution times for the test described in this section, summarized in Fig. 25, are similar to the Hornung test ones, see Fig. 12. The execution time spent to solve the kinetics is about the $\frac{17}{18} 100 = 94.4\%$ of the total execution time, slightly less than the previous, but similar enough to let us say that, in our numerical model, such ratio is independent of both the domain structure and the initial conditions.

Similarly to the previous test case, we have repeated the simulations using either a single-GPU or two-GPUs (system in Table A.3) with Grid 1, see Fig. 15, and a finer grid, Grid 2, obtained doubling the number of cells in the j -direction. For both grids, Fig. 26 provides the GPU execution time as a function of the advection time steps. In this case, the use of two GPUs allows us to obtain a time reduction of about 30% with respect to the case of a single GPU, almost independently of the mesh, see Fig. 26. This result is not particularly satisfactory being not in line with the performance obtained for the case of a perfect gas [23]. Such a performance degradation is due to the implementation used to transfer the boundary conditions between blocks running on different GPUs. In fact, the heavy contribution to the total execution time due to boundary conditions calculation (BC), more evident when 2 GPUs are used, is shown in Fig. 27, where detailed contributions of the other main subroutines are also reported.

The execution time of a subroutine, called *fname*, is measured by the standard C *clock()* function and by two variables *tm_fname_i* and *tm_fname* according to the following scheme:

```
tm_fname_i=clock();
Subroutine content;
tm_fname +=((REAL)(clock()-tm_fname_i)/CLOCKS_PER_SEC);
```

where the type *REAL* can be chosen as *double* or *float*.

In more detail, data transfer between Domain 1 and Domain 2, managed by devices *devGPU[1]* and *devGPU[2]* respectively, is enabled at first by a single call of the function *cudaDeviceEnablePeerAccess*, as follows:

```
cudaSetDevice(devGPU[1]);
cudaDeviceEnablePeerAccess(devGPU[2],0);
cudaSetDevice(devGPU[2]);
cudaDeviceEnablePeerAccess(devGPU[1],0);
```

Subsequently, at each advection step, data are exchanged among the devices, by *m* calls of the function *cudaMemcpy(array_destination[], array_origin[], Lenght*sizeof(double), cudaMemcpyDefault)*, where *m* is almost proportional to the number of cells along the boundary joining Domain 1 and Domain 2 and the value of the integer parameter *Lenght* depends on how the data to be exchanged are arranged in *array_destination* and *array_origin*. Such an implementation turned out to be effective in the case of perfect gas; however, for the present case of reacting flow with a large number of species, a proper arrangement of the domain decomposition and management of ghost cell memory passage among GPUs could enhance multi-GPU performance.

7. Conclusions

This paper presents the most advanced results obtained in the aim to extend the state-to-state kinetics to simulate complex 2D/3D configurations. It was possible to achieve these results by the aid of the most advanced technology in the computer design. Graphic Processing Units (GPU), designed for high speed and high quality computer graphics, is being used for high performance calculations. GPU's have thousand of small processors, and are particularly suitable for simple calculations. This powerful tool allows one to perform heavy calculations on desktop machines speeding-up the execution of one or two orders of magnitude with respect to the CPU version of the same algorithm. In this paper, this result has been achieved solving the 2D unsteady Euler equations by means of an explicit scheme and employing an operator splitting approach to solve the kinetic equations.

With this technique, we are able to investigate problems which are usually avoided because the computational resources are too high for common calculations. In particular, we have investigated 2D models of hypersonic wind tunnels (including the obstacle) using the state-to-state approach to calculate the vibrational distributions of diatomic molecules. In the past this approach was limited to 1D calculations, putting in evidence the role of non-equilibrium distributions in affecting the behaviors of high enthalpy flows. However, extension to realistic 2D or 3D geometries is considered prohibitive [15], limiting the interest in the state-to-state model in the aerospace community. The calculations here presented show the feasibility of 2D state-to-state models, opening new frontiers not only in the field of hypersonics, but also in a large class of devices where the interaction of a plasma with the surrounding environment is a critical aspect. The approach here described will be extended to more complex mixtures like air and to molecules like CO_2 [41] with few thousands of levels.

Acknowledgments

The authors would like to thank the following persons:

- Prof. Massimo Bernaschi, chief technology officer of the Institute for Applied Computing at Italy's CNR and CUDA fellow since 2012, for his generous help in remote using of the recent GeForce GTX TITAN and Tesla K20c.
- Dr. Giacinto Donvito of the "INFN" - Bari (Italy) for needful support in remote using of the GPUs Tesla C2070.

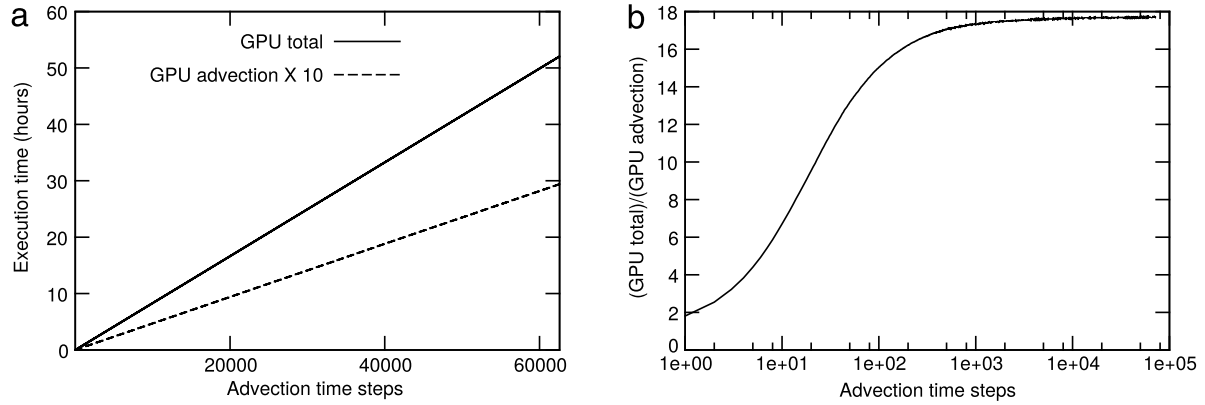


Fig. 25. GPU execution times as a function of the advection time steps: (a) total (solid line) and advection times ten (dashed line); (b) ratio (total)/(advection).

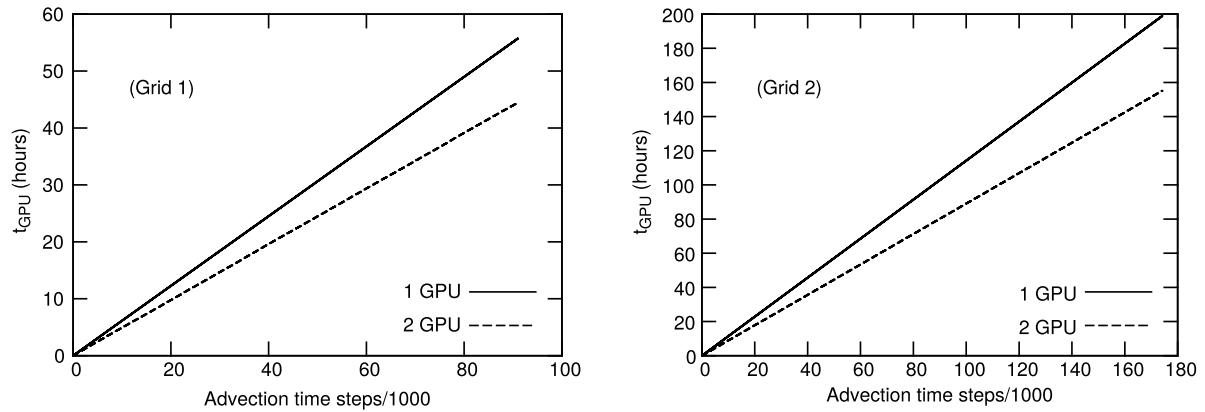


Fig. 26. GPU execution time as a function of the advection time steps, for the Grid 1 (Left) and the Grid 2 (Right): simulation performed by a single-GPU and two-GPU belonging to the system shown in Table A.3; the comparison is presented for the overall time.

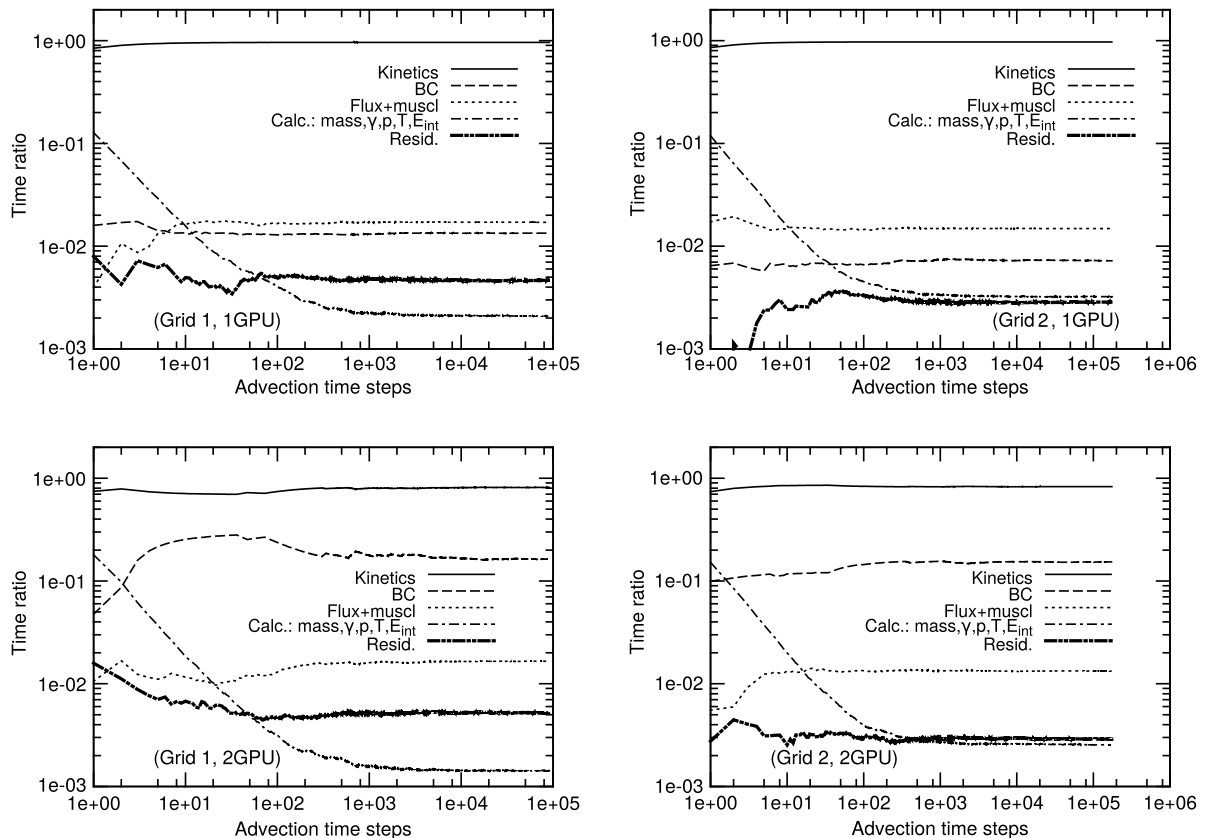


Fig. 27. Execution time of the main subroutines, nondimensionalized with respect to the total execution time, as a function of advection time steps; the comparison is presented for all the combinations: Grid 1 / Grid 2 and single-GPU / two-GPUs.

Appendix. CUDA resources employed: GPU devices and CUDA toolkits

Every computation performed in this paper has used a specific GPU-CPU-(CUDA Toolkit) configuration, which in turn was selected among those listed in Tables A.1–A.3.

Table A.1

2 × GPU basic hardware and CUDA Toolkit, provided by the INFN, “Dipartimento Interateneo di Fisica”-Bari (thanks to dr. Giacinto Donvito).

GPU:	2 × Tesla C2070
CUDA Capability:	2.0
Global memory:	5,375 MB
MP × Cores/MP = Cores:	14 × 32 = 448
Constant memory:	65,536 bytes
Shared memory per block:	49,152 bytes
Registers per block:	32,768
Warp size:	32
Max threads per block:	1,024
Max sizes of a block:	1,024 × 1,024 × 64
Max sizes of a grid:	65,535 × 65,535 × 65,535
Chip clock rate:	585 MHz
Memory clock rate:	1.49 GHz
CPU:	Intel(R) Xeon(R) E5620
Clock rate:	2.40 GHz
RAM:	24.00 GB
CUDA compilation tools:	release 5.0, V0.2.1221

Table A.2

Single GPU basic hardware and CUDA Toolkit, provided by the CNR, IAC Roma (thanks to prof. Massimo Bernaschi).

GPU:	Tesla K20c
CUDA Capability:	3.5
Clock rate:	705,500 Hz
Global memory:	5 GB
MP × Cores/MP = Cores:	13 × 192 = 2496
Constant memory:	65,536 bytes
Shared memory per MP:	49,152 bytes
Registers per MP:	65,536
Threads in warp:	32
Max threads per block:	1,024
Max sizes of a block:	1,024 × 1,024 × 64
Max sizes of a grid:	2147,483,647 × 65,535 × 65,535
CPU:	Intel(R) Xeon(R) CPU E5-2609
Clock rates:	1.20 GHz
Cache size:	10,240 KB
CUDA Toolkit:	release 5.5

Table A.3

2 × GPU basic hardware and CUDA Toolkit, provided by the cluster of the “Politecnico di Bari”.

GPU:	Tesla K40m
CUDA Capability:	3.5
Clock rate:	745,000 Hz
Global memory:	3.2 GB
MP × Cores/MP = Cores:	15 × 192 = 2880
Constant memory:	65,536 bytes
Shared memory per MP:	49,152 bytes
Registers per MP:	65,536
Threads in warp:	32
Max threads per block:	1,024
Max sizes of a block:	1,024 × 1,024 × 64
Max sizes of a grid:	2,147,483,647 × 65,535 × 65,535
CPU:	Intel(R) Xeon(R) CPU E5-2640 v2
Clock rates:	2.00 GHz
Cache size:	20,480 KB
CUDA Toolkit:	release 5.5

References

- [1] C. Park, Nonequilibrium Hypersonic Aerothermodynamics, John Wiley & Sons, 1990.
- [2] M. Capitelli, et al., Fundamental Aspects of Plasma Chemical Physics: Kinetics, first ed., in: Atomic, Optical, and Plasma Physics, Springer, New York, 2015.
- [3] M. Capitelli, G. Colonna, G. D'Ammando, V. Laporta, A. Laricchiuta, Phys. Plasmas (1994-present) 20 (10) (2013) 101609.
- [4] M. Capitelli, G. Colonna, G. D'Ammando, V. Laporta, A. Laricchiuta, Chem. Phys. 438 (2014) 31–36.
- [5] G. Colonna, V. Laporta, R. Celiberto, M. Capitelli, J. Tennyson, Plasma Sources Sci. Technol. 24 (3) (2015) 035004.
- [6] I. Armenise, M. Capitelli, G. Colonna, N. Koudriavtsev, V. Smetanin, Plasma Chem. Plasma Process. 15 (3) (1995) 501–528.
- [7] G. Colonna, M. Tuttafesta, D. Giordano, Comput. Phys. Comm. 138 (3) (2001) 213–221. [http://dx.doi.org/10.1016/S0010-4655\(01\)00211-9](http://dx.doi.org/10.1016/S0010-4655(01)00211-9), <http://www.sciencedirect.com/science/article/pii/S0010465501002119>.
- [8] G. Colonna, M. Tuttafesta, M. Capitelli, J. Thermophys. Heat Transfer 14 (2000) 455–456.
- [9] G. Colonna, G. D'Ammando, L. Pietanza, M. Capitelli, Plasma Phys. Control. Fusion 57 (1) (2015) 014009.
- [10] G. Colonna, L. Pietanza, G. D'Ammando, Chem. Phys. 398 (2012) 37–45.
- [11] G. Colonna, M. Capitelli, D. Giordano, M. Tuttafesta, J. Thermophys. Heat Transfer 13 (1999) 372–375. <http://dx.doi.org/10.2514/2.6448>.
- [12] G. Colonna, L.D. Pietanza, M. Capitelli, J. Thermophys. Heat Transfer 22 (2008) 399–406.
- [13] G. Colonna, M. Tuttafesta, M. Capitelli, D. Giordano, 21th Symposium on Rarefied Gas Dynamics, 1999, pp. 281–288.
- [14] D. Giordano, V. Bellucci, G. Colonna, M. Capitelli, I. Armenise, C. Bruno, J. Thermophys. Heat Transfer 11 (1997) 27–35.
- [15] L. Cutrone, M. Tuttafesta, M. Capitelli, A. Schettino, G. Pascasio, G. Colonna, Proceedings of the 29th International Symposium on Rarefied gas Dynamics, vol. 1628, AIP Publishing, 2014, pp. 1154–1161.
- [16] S. Gimelshein, M. Ivanov, G. Markelov, Y. Gorbachev, S. Gimelshein, M. Ivanov, G. Markelov, Y. Gorbachev, Statistical Simulation of Nonequilibrium Rarefied Flows with Quasiclassical VVT Transition Models, American Institute of Aeronautics and Astronautics, 1997.
- [17] D. Bruno, M. Capitelli, S. Longo, P. Minelli, F. Taccogna, Plasma Sources Sci. Technol. 12 (4) (2003) S89–S97. <http://dx.doi.org/10.1088/0963-0252/12/4/024>, cited By 2. <http://www.scopus.com/inward/record.url?eid=2-s2.0-0345015533&partnerID=40&md5=a892ed3ab1e1dbccb2d00c06a226d8b7>.
- [18] D. Andrienko, I.D. Boyd, Chem. Phys. 459 (2015) 1–13. <http://dx.doi.org/10.1016/j.chemphys.2015.07.023>, <http://www.sciencedirect.com/science/article/pii/S0301010415002141>.
- [19] P. Valentini, T.E. Schwartzentruber, J.D. Bender, I. Nompelis, G.V. Candler, Phys. Fluids (1994-present) 27 (8) (2015) 086102.
- [20] G. Colonna, M. Capitelli, J. Phys. D: Appl. Phys. 34 (12) (2001) 1812. <http://stacks.iop.org/0022-3727/34/i=12/a=308>.
- [21] A. Guy, A. Bourdon, M.-Y. Perrin, Chem. Phys. 420 (2011) 15–24.
- [22] T.E. Magin, M. Panesi, A. Bourdon, R.L. Jaffe, D.W. Schwenke, Chem. Phys. 398 (2012) 90–95.
- [23] M. Tuttafesta, G. Colonna, G. Pascasio, Comput. Phys. Comm. 184 (2013) 1497–1510.
- [24] H. Le, J. Cambier, AIAA 2012-0721, <http://arxiv.org/abs/1110.4903> arXiv:1110.4903.
- [25] H.P. Le, J.-L. Cambier, L.K. Cole, Comput. Phys. Comm. 184 (3) (2013) 596–606. <http://dx.doi.org/10.1016/j.cpc.2012.10.013>, <http://www.sciencedirect.com/science/article/pii/S0010465512003463>.
- [26] K.E. Niemeyer, C.-J. Sung, J. Comput. Phys. 256 (2014) 854–871. <http://dx.doi.org/10.1016/j.jcp.2013.09.025>, <http://www.sciencedirect.com/science/article/pii/S0021999113006396>.
- [27] B. Grossman, P. Cinnella, Comput. Struct. 30 (1988) 79–93.
- [28] B. Grossman, P. Cinnella, J. Comput. Phys. 88 (1990) 131–168.
- [29] R.P. Fedkiw, A survey of chemically reacting, compressible flows (Ph.D. thesis), University of California - Los Angeles, 1997.
- [30] G. Colonna, M. Tuttafesta, M. Capitelli, D. Giordano, J. Thermophys. Heat Transfer 14 (3) (2000) 455–456.
- [31] G. Colonna, M. Tuttafesta, M. Capitelli, D. Giordano, in: R. Brun, R. Campargue, R. Gatignol, J.-C. Lengrand (Eds.), 21th International Symposium on Rarefied Gas Dynamics, vol. 2, 1999, pp. 281–288.
- [32] F. Esposito, I. Armenise, M. Capitelli, Chem. Phys. 331 (1) (2006) 1–8.
- [33] W. Ran, W. Cheng, F. Qin, X. Luo, J. Comput. Phys. 230 (2011) 8797–8812.
- [34] J.L. Steger, R. Warming, J. Comput. Phys. 40 (2) (1981) 263–293.
- [35] C. Hirsch, Computational Methods for Inviscid and Viscous Flows, Vol. 2, Butterworth-Heinemann, 2007.
- [36] W.H. Press, S.A. Teukolsky, W.T. Vetterling, B.P. Flannery, Numerical Recipes in C (2nd ed.): the Art of Scientific Computing, Cambridge University Press, New York, NY, USA, 1992.
- [37] S.P. Sharma, S.M. Ruffin, W.D. Gillespie, S.A. Meyer, J. Thermophys. Heat Transfer 7 (4).
- [38] H.G. Hornung, J. Fluid Mech. 53 (1972) 149–176.
- [39] M.N. Macrossan, J. Comput. Phys. 80 (1989) 204–231.
- [40] G. Tchuén, Y. Bartschell, Physico - Chemical Modelling in Nonequilibrium Hypersonic Flow Around Blunt Bodies, InTechOpen, 2011, pp. 125–159 (Chapter 5).
- [41] I. Armenise, E. Kustova, Chem. Phys. 415 (2013) 269–281.